Source term determination with elastic plume bias correction

Ondřej Tichý [a],[*], Václav Šmídl [a], Nikolaos Evangeliou [b]

[a] *The Czech Academy of Sciences, Institute of Information Theory and Automation, Prague, Czech Republic*
[b] *NILU: Norwegian Institute for Air Research, Kjeller, Norway*

ARTICLE INFO

ABSTRACT

Estimation of a source term, i.e. release rate, of atmospheric radionuclide emissions is of key interest for nuclear emergency response and further accident analysis. The source term estimate is, however, often very inaccurate due to biases in atmospheric transport and used meteorological analysis. We propose a method for atmospheric plume bias correction which uses not only concentrations modeled at a measuring site but also the information on concentration gradient from the neighborhood of each measuring site, i.e. information already available from the atmospheric transport model. To properly regularize the model, we propose an elastic model of the plume bias correction based on regularization with the use of known topology of the measurement network. The proposed plume bias correction method can be coupled with an arbitrary source term estimation algorithm and can be instantly applied to any other atmospheric release of hazardous material. We demonstrate the method in two real cases. First, we use data from the European Tracer Experiment to validate the methodology. Second, we use data from the [106]Ru occurrence over Europe in 2017 to demonstrate the methodology in a more demanding case where agreement with state-of-the-art estimates is shown with much better reconstruction of measurements.

1. Introduction

The accidental release of hazardous materials can have serious impact on environment. Particularly important and of public interest are atmospheric releases of radioactive materials, especially after Chernobyl and Fukushima Daiichi nuclear accidents (Evangeliou et al., 2017; Katata et al., 2012; Li et al., 2019). Therefore, smaller releases such as iodine-131 releases (Masson et al., 2018; Tichý et al., 2017), ^{75}Se release (De Meutter and Hoffman, 2020), or recent [106]Ru release (Saunier et al., 2019; Tichý et al., 2021) raised also significant interest of public and scientific community. To trace the consequences of accidental releases, it is of great importance to know the source term of emission, i.e. its temporal release rates. When the source term can not be measured or estimated from core information (i.e., bottom-up methods), inverse approach can be employed where differences between the measurements and the atmospheric model predictions are optimized under domain-specific assumptions.

The source term estimations rely on two key aspects, the atmospheric transport model (ATM) (Leelőssy et al., 2018) coupled with selected meteorological data and the used source term estimation method (Hutchinson et al., 2017). For accidental atmospheric releases of radioactive materials, the standard approach is the linear approximation of the problem with source-receptor sensitivity (SRS) matrix calculated using the ATM describing the response of the measurement on the given time interval to the unit release (Seibert, 2001; Seibert and Frank, 2004). Assuming measurements aggregated in column vector $\mathbf{y}$, SRS matrix $\mathbf{M}$, and the source term in column vector $\mathbf{x}$, the linear relationship is expressed as

$$\mathbf{y} = \mathbf{Mx}. \tag{1}$$

However, the relation may be significantly inaccurate due to uncertainties associated with ATM bias caused by, e.g., uncertainties in meteorological data (Leelőssy et al., 2017; Sørensen et al., 2020; De Meutter et al., 2021), uncertainties in ATM parametrization (Bocquet, 2012; Ganesan et al., 2014; Mao et al., 2020; Ling et al., 2021), spatial quality of monitoring network (Tichý et al., 2017), or measurements processing (Kumar et al., 2020). Inaccurate prediction of the matrix $\mathbf{M}$ results in biased estimate of the source term $\mathbf{x}$. Biases in the ATM model are the key reasons for discrepancies in estimated source terms for different model settings, see e.g. iodine release in 2011 (Tichý et al., 2017) or ruthenium release in 2017 (Dumont Le Brazidec et al., 2021; Tichý et al., 2021), as well as for discrepancies between model predicted values and measurements, see e.g. iodine release in 2017 (Masson et al., 2018) or Chernobyl source term (Evangeliou et al., 2017).

The majority of inversion methods focuses on modeling the stochastic error between the measurements and the model predictions. The likelihood of this error is often chosen as Gaussian (Saunier et al., 2013; Zhang et al., 2017; Zhang and Huang, 2017; Tichý et al., 2020) or recently as log-normal (Liu et al., 2017; Dumont Le Brazidec et al., 2020) or as other logarithm-based distributions (Dumont Le Brazidec et al., 2021) to compensate the mismatch. Although various parametrizations of covariance matrix and various estimation schemes have been employed, they can essentially compensate only specific aspects since they do not address the true source of the mismatch which is the SRS matrix.

A more direct approach to correct the SRS matrix is to estimate corrections of the input parameters of the ATM such as scaling of wet scavenging and dry deposition (Bocquet, 2012), dispersion coefficients (Mao et al., 2020, 2021), or wind speed (Krysta et al., 2006; Kovalets et al., 2009). The wind speed perturbation was also used within ensemble Kalman Filter framework (Zhang et al., 2015) to lower the bias caused by the meteorological data and estimate the emission rate simultaneously. In such approaches, the SRS matrix is still generated from the ATM with perturbed input which is advantageous for regularization of the inversion problem, but may become too rigid when more complex modifications of the weather conditions are required. Moreover, the inference procedure is typically computationally expensive due to required interactions with the ATM.

More flexible approach bypassing the ATM model for SRS matrix correction was proposed by Li et al. (2018)) where the right side of Eq. 1 is preconditioned by the diagonal matrix with coefficients to be estimated besides the source term. This approach is similar to estimation of the measurement error and is reliable only if the majority of the measurements are correct (Martinez-Camara et al., 2014). An improvement of this approach was proposed recently by Fang et al. (2021)) where a better preconditioning of the right side of Eq. 1 is proposed based on the work of Ganesan et al. (2014)). In the latter, the correlation matrix is constructed based on spatial distance between every pair of measurements positions with automatically calculated autocorrelation scale. Both methods were tested on wind tunnel experiments with interesting performance. However, these plume bias correction methods rely only on the measurements and point predictions of the concentrations without any additional information for the ATM.

The basic idea of our approach to plume bias correction is to combine the measurements with some elementary information from the ATM without the need of too many ATM runs and without the assumption that the ATM is correct. Specifically, we propose to use the ATM to estimate the sensitivity with respect the predicted concentration for each measurement. Moreover, we assume that any measurement can be associated with a concentration predicted only in the limited spacial and temporal neighborhood. This also means that we seek only local corrections of the concentration predictions of an ATM, not correction of the ATM parameters that would provide correction of the spatial distribution of concentrations for the whole domain. The method do not interact with an ATM and is much more computationally effective. The interpretation of our bias correction at each point is then represented by a shift in space and time corresponding to temporal and spacial displacement of the predicted concentrations.

The proposed plume bias correction is highly over-parametrized and the challenge is to design a realistic regularization that allows stable estimation. We design the regularization using two principles: (i) the correction should be zero if the measurement is withing observation noise, and (ii) the correction vector of two nearby measurements should be similar (i.e. correlated). The second assumption is commonly used for measurement noise correlations (Ganesan et al., 2014), however we further relax it to allow for unknown correlation coefficients. The regularization is based on similar principles such as sparsity and smoothness prior in source term determination (Tichý et al., 2016).

The proposed model intends to improve the source term estimate using correction of the SRS matrix. The model is in essence a bi-linear model, i.e. linear in plume bias correction for known release, and linear in release for known bias correction. The Variational Bayes method has been shown to be an effective tool for such models (Smidl and Quinn, 2006). It results in an iterative algorithm alternating two essential steps: i) plume bias correction, and ii) source term determination. Due to this algorithmic structure, we can study performance of the proposed bias correction model in combination with established source term determination methods. Specifically, we will study source term determination using an optimization approach (Eckhardt et al., 2008), and the least-square with adaptive prior covariance (LSAPC) method (Tichý et al., 2016).

The proposed method is validated on source term determination from data from the European tracer experiment (ETEX) (Nodop et al., 1998) with the use of HYSPLIT atmospheric transport model. Then, the performance of the method is tested on recent ^{106}Ru release over Europe in 2017 (Masson et al., 2019) with the use of FLEXPART atmospheric transport model.

1.1. Layout of the paper

The rest of the paper is organized as follows. Section 2 is devoted to the formulation of the bilinear inverse problem and elastic plume bias correction model. The definition of the bilinear inverse problem and intuitive outlook on plume bias correction are given in Section 2.1. Section 2.2 propose elastic regularization of the bias correction using measurement network topology while its rigorous formulation using prior model is given in Section 2.3 and its variational Bayes solution in Section 2.4. Due to the modular structure of the plume bias correction method, arbitrary linear inverse method can be coupled with it as shown in Section 2.5. The experimental validation is given in Section 3 where the ETEX experiment is studied in Section 3.1 and the case of ^{106}Ru release in 2017 is studied in Section 3.2. Conclusions are given in Section 4.

2. Materials and Methods

We follow the concept of source-receptor-sensitivity (SRS) matrix which is used in a wide range of applications in regional or continental scale scenarios for linear inverse modeling (Seibert and Frank, 2004; Li et al., 2018; Fang et al., 2021). In this concept, the linear relationship is assumed between the source and the receptor as $m_{ij} = \frac{\hat{c}_{ij}}{\overline{x}_j}$, where $\overline{x}_j$ is the simulated activity of a release pulse at time j from the site, and $\hat{c}_{ij}$ is the calculated response for this release at the ith measurement. Denoting spatial coordinates of the ith measurement $s_{h,i}$, $s_{v,i}$ (longitudinal and latitudinal) and time interval of the measurement t_i, the predicted concentration $\hat{c}_{ij}$ is evaluated as a discrete point in the 3D concentration field c_j, i.e. $\hat{c}_{ij} = c_j(s_{h,i}, s_{v,i}, t_i)$, of the jth simulation. The concentration measurement y_i can thus be explained as a superposition of concentrations from all elements of the source term $\mathbf{x}$ weighted by the model-predicted m_{ij}, aggregated in the matrix $\mathbf{M}$, summarized in matrix notation in Eq. 1.

Note that, in this notation, the symbol y_i refers to the ith measurement at given location and for given time period. We assume to have p measurements in total, aggregating several measurements from multiple locations.

2.1. Bilinear inverse model formulation

In this subsection, we are concerned with modeling of the inverse problem with bias in the plume model. Specifically, we assume that the ATM is not accurate and the plume model is shifted in both space and time from the reality. Then, the measurement y_i should not be matched with concentration evaluated at the nominal coordinates but at the shifted coordinates

$$\widetilde{c}_{ij} = c_j(s_{h,i} + h_{h,i}, s_{v,i} + h_{v,i}, t_i + h_{t,i}), \tag{2}$$

where $h_{h,i}$, $h_{v,i}$ are longitudinal and latitudinal components of the *bias correction*, and $h_{t,i}$ is the temporal component of the bias correction at the ith sensor. Naturally, the bias is not known and we aim to estimate it from the data, estimating three biases for each sensor $\mathbf{h} = [\mathbf{h}_h, \mathbf{h}_v, \mathbf{h}_t]$, forming the *bias correction field*.

Estimating the bias from the full numerical model 2 would be too expensive. Therefore, we propose to linearize the concentration field in the close neighborhood of the ith measurement by the Taylor expansion yielding a linear model

$$\widetilde{c}_{ij} \approx \hat{c}_{ij} + h_{h,i}\frac{\partial c}{\partial s_h} + h_{v,i}\frac{\partial c}{\partial s_v} + h_{t,i}\frac{\partial c}{\partial t}, \tag{3}$$

where $\hat{c}_{ij}$ is the nominal prediction of the measurement (without correction). Calculation of the derivative is further approximated by finite difference estimates:

$$\widetilde{c}_{ij} \approx \hat{c}_{ij} + h_{h,i}\Delta c_{h,i} + h_{v,i}\Delta c_{v,i} + h_{t,i}\Delta c_{t,i},$$
$$\Delta c_{h,i} = \frac{c(s_{h,i} + \Delta s_h, s_{v,i}, t_i) - c(s_{h,i} - \Delta s_h, s_{v,i}, t_i)}{2\Delta s_h}, \tag{4}$$

where Δs_h is the chosen discretization step in the longitudinal location of the receptor. The differences $\Delta c_{v,i}$ and $\Delta c_{t,i}$ are obtained analogically using discretization steps Δs_v and Δt. Since positions of the measurements are known, we can pre-compute the required differences together with nominal values of the concentrations in the form of SRS matrices.

Replacing the default prediction by the bias-corrected version yields a new matrix $\widetilde{\mathbf{M}}$, where $\widetilde{m}_{ij} = \frac{\widetilde{c}_i}{\overline{x}_j}$ with unit release $\overline{x}_j$ at time j, in complete analogy to the linear definition:

$$\mathbf{y} = \widetilde{\mathbf{M}}\mathbf{x} + \mathbf{e}, \tag{5}$$

$$\widetilde{\mathbf{M}} = \mathbf{M} + \mathbf{H}_h\mathbf{M}_h + \mathbf{H}_v\mathbf{M}_v + \mathbf{H}_t\mathbf{M}_t. \tag{6}$$

Here, we have restructured the definition 4 to the matrix form, using the original matrix $\mathbf{M}$ and new sensitivity matrices $\mathbf{M}_h$, $\mathbf{M}_v$, $\mathbf{M}_t$. The sensitivity matrix to longitudinal space correction is defined as $m_{h,ij} = \frac{\Delta c_{h,i}}{\overline{x}_j}$. The sensitivity matrices with latitudinal gradients and temporal gradients, $\mathbf{M}_v$ and $\mathbf{M}_t$, are obtained analogically. Form 4 is then obtained by sum of $\mathbf{M}$ with sensitivity matrices $\mathbf{M}_h$, $\mathbf{M}_v$, $\mathbf{M}_t$ multiplied by correction terms

$$\mathbf{H}_h = \text{diag}(\mathbf{h}_h) = \begin{pmatrix} h_{h1} & & & \\ & h_{h2} & & \\ & & \ddots & \\ & & & h_{hp} \end{pmatrix}, \tag{7}$$

which is the diagonal matrix representing bias correction shifts of the concentration field at each measurement which need to be estimated. Matrices $\mathbf{H}_v = \text{diag}(\mathbf{h}_v)$, and $\mathbf{H}_t = \text{diag}(\mathbf{h}_t)$ are analogous matrices representing shifts in the latitudinal and temporal dimension.

Remark 1(Bilinear model): Note that the model 5 is bilinear; it means that with known variables $\mathbf{H}_h$, $\mathbf{H}_v$, and $\mathbf{H}_t$ (forming the corrected SRS matrix $\widetilde{\mathbf{M}}$), the model is linear in variable $\mathbf{x}$ and with known $\mathbf{x}$, the model is linear in $\mathbf{h}$. General estimation methods of such models typically use iterations of two steps solving individual linear problems independently. Hence, any inverse method of source term estimation may be coupled with bias correction estimation. Note however, that the number of unknowns in $\mathbf{h}$ is three times higher than the number of observations. Estimation of its values is thus strongly determined by the used regularization.

2.1.1. Intuitive explanation of the model

The idea of local correction of the bias field is illustrated in Fig. 1 on the case of measured concentration $y_i = 0.55$ and model predicted

concentration $c_i = 0.33$. Since these two values are the only information for the linear model, the two cases depicted in Fig. 1 are for this model identical. However, the proposed model takes into account the local shape of the concentration. If the concentration profile is sharp as in Fig. 1 left, a small shift of the concentration model to the left can significantly minimize the mismatch between the model and measurement. On the other hand, if the concentration profile in the neighborhood is flat, a shift of the model does not improve the mismatch significantly. The additional information about local derivative of the concentration (stored in matrices $\mathbf{M}_h$, $\mathbf{M}_v$, $\mathbf{M}_t$), via the local gradient Δc, Eq. 4, is thus essential in distinguishing these two cases. While in the first, only a small shift is sufficient to minimize the error of the fit, in the second case, even a shift by a maximum allowed distance $h_h = \Delta s_h$ is not sufficient. The maximum allowed shift serves as a regularization term for preventing arbitrary shifts of the concentration field.

2.1.2. Practical computation of bi-linear model inputs

To summarize the input to the proposed bilinear model, we assume the availability of simulated concentrations also around each measuring site as an ATM output. In this case, we assume the simplest topology in the form of cross with the center in the receptor and shoulders in the east, west, south, and north, see Fig. 2 for illustration of one measuring site. In addition, we naturally assume the knowledge of concentrations shifted for one step in time backward and forward. These concentrations can be calculated in both, backward or forward, modes of an ATM. While all concentrations are already available for forward mode, there is need for six additional runs of an ATM in backward mode, four runs for shifted locations and two runs for temporal shift.

To obtain gradient matrices ($\mathbf{M}_h$, $\mathbf{M}_v$, $\mathbf{M}_t$), we compute SRS matrices from concentrations with east-shifted location, i.e. $m_{\text{east},ij} = \frac{c(s_{h,i}+\Delta s_h, s_{v,i}, t_i)}{\overline{x}_j}$, and west-shifted locations, i.e. $m_{\text{west},ij} = \frac{c(s_{h,i}-\Delta s_h, s_{v,i}, t_i)}{\overline{x}_j}$. These matrices are subtracted yielding longitudinal gradient matrix $\mathbf{M}_h = \frac{1}{2\Delta s_h}(\mathbf{M}_{\text{east}} - \mathbf{M}_{\text{west}})$. The SRS matrices for latitudinal and time directions, i.e. south-shifted, north-shifted, backward-time-shifted, and forward-time-shifted, forming matrices $\mathbf{M}_v$ and $\mathbf{M}_t$, are obtained analogically.

2.2. Elastic regularization of the bias correction field

The core of our proposed method is to estimate the correction bias $\mathbf{h}$ from the data. Since the number of unknowns is greater than the number of observations, the model has to be regularized. We propose two principles for its regularization:

1. the bias correction for each measurement is bounded to a fixed interval

$$h_{h,i} \in [-\Delta s_h, +\Delta s_h], h_{v,i} \in [-\Delta s_v, +\Delta s_v],$$
$$h_{t,i} \in [-\Delta t, +\Delta t], \forall i \tag{8}$$

2. the bias corrections of neighboring sensors are correlated with unknown correlation coefficients.

These two principles will be first illustrated for intuition, and later formalized using prior distributions. Soft correlation allows the bias corrections to behave like an elastic material, the move of the bias is greater with sufficiently high "pull" by the data.

We have tested that using only the assumption of the maximum allowed shift 8 is not a sufficient regularization, since the space of available corrections is too large. Therefore, we add the assumption of correlations the meaning of which is illustrated in Fig. 3 using contour plot of the concentration predicted by the model (full line) and true concentration field (dashed line), from which the measurements are taken. The colors at the measured point (full circles) corresponds to
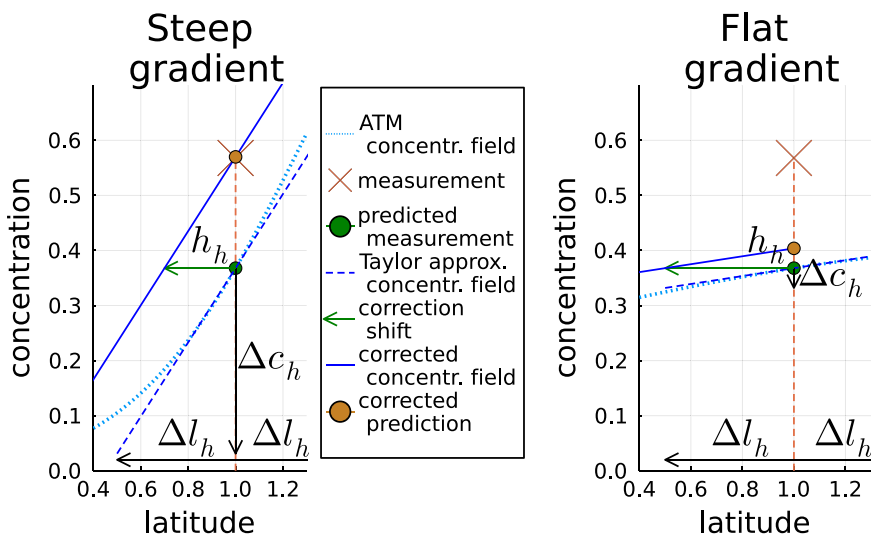
Fig. 1. Illustration of the value of information about the shape of the concentration field in the neighborhood of the measurements.
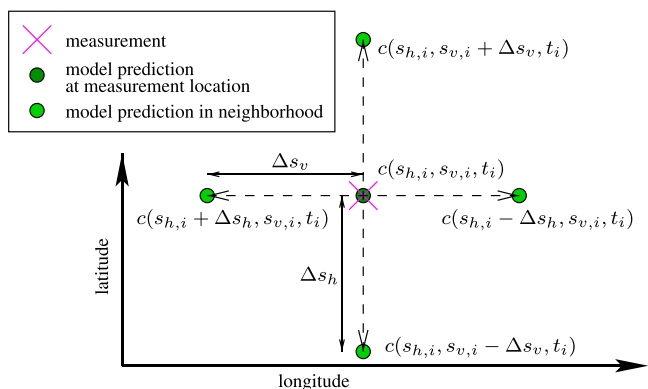

Fig. 2. Illustrative example of one measuring site and information from its surrounding.

colors of the dashed contours of the true concentration field on which they lie (i.e. blue and black). Following the Taylor expansion, we approximate the concentration at the sensor by a plane, with the gradient visualized by a dotted line. Under the assumption of independent correction vectors, the correction vector would lie on the gradient, Fig. 3 top, pointing at different directions. However, if we impose strong correlation (i.e. that all vectors have to be the same), the correction vectors align in the right solution, i.e. the correction vectors denote the shift of the prediction model to match the measurements.

Naturally, the assumption of the identical correction vectors is unrealistic and the correlation factor has to be relaxed. This is commonly done using decaying with distance (Ganesan et al., 2014)) and many later works. However, it still prescribes the form of the correlation and relies on tuning parameter. We propose to relax the form of the correlation coefficients, estimate them from the data using prior similar to the Bayesian sparsity and smoothness prior (Tichý et al., 2016). The effect of this choice is that the correlation is estimated to be very strong where the data allows for it, but it may be completely independent if the data do not fit this assumption. This principle intuitively corresponds to behavior of an elastic material, hence we denote it *elastic* regularization.

In the next section, we will formulate the rigorous prior model for the SRS field correction coefficients $\mathbf{h}_h$, $\mathbf{h}_v$, and $\mathbf{h}_t$ which formalizes all discussed assumptions.
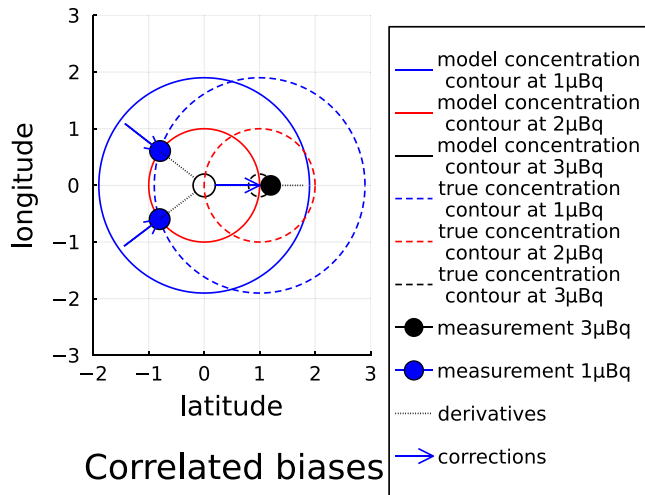

Fig. 3. Illustration of independent bias correction and correlated bias correction of the concentration field in the neighborhood of the measurements.

2.3. Complete probabilistic model

In this Section, we define all components of the probabilistic model, the likelihood (data fitting) and the prior (regularization). Prior distribution is also assigned to all tuning parameters since they will be also

estimated from the data using the power of the Bayesian approach.

The observation model is selected to be the very standard mean-square error, which corresponds to Gaussian likelihood

$$p(\mathbf{y}|\mathbf{x}, \omega, \mathbf{h}_h, \mathbf{h}_v, \mathbf{h}_t) = \mathcal{N}\left(\mathbf{y}\Big|\widetilde{\mathbf{M}}\mathbf{x}, \omega^{-1}I_p\right) \tag{9}$$

The model introduced scalar variable ω which serves as the observation noise precision (extension to a known general covariance matrix is straightforward). The measurement precision is considered to be unknown, thus, we propose to choose its prior model to be conjugate to the observation model 9 using Gamma distribution as

$$p(\omega) = \mathcal{G}(\omega|\vartheta_0, \rho_0), \tag{10}$$

where ϑ_0, ρ_0 are scalar prior constants that serve as numerical stabilizers and are set to non-informative 10^{-10}.

2.3.1. Bias correction field regularization via elasticity

The key ingredient of the method is models of vectors $\mathbf{h}_h$, $\mathbf{h}_v$, and $\mathbf{h}_t$ which are the weighting factors of the gradient matrices $\mathbf{M}_h$, $\mathbf{M}_v$, and $\mathbf{M}_t$. For conciseness, we explain design of the prior for vector $\mathbf{h}_h$, the remaining are analogous.

Probability of the whole vector can be written as product of probabilities of each elements using the chain rule of probability

$$p(\mathbf{h}_h) = p(h_{h1}|h_{h2}, \ldots h_{hp})p(h_{h2}|h_{h3}, \ldots h_{hp})\ldots p(h_{hp}), \tag{11}$$

and proposing model for each factor $p(h_{hi}|h_{hi+1}\ldots h_{hp})$. Since we assume that the correlation is non-zero only in the neighborhood of the ith measurement, we impose conditional independence

$$p(h_i|h_{i+1}, \ldots h_p) \equiv p(h_i|\widetilde{\mathbf{h}}_i), \widetilde{\mathbf{h}}_i = [h_j : j \in \mathscr{I}_i] \tag{12}$$

where $\mathscr{I}_i \subset \{i+1, \ldots, p\}$ is the set of indexes of measurements that are in the spacial or temporal neighborhood of the ith measurement. This neighborhood is the same for longitudinal, latitudinal and temporal bias. Note that the number of elements n_i of $\mathscr{I}_i$ varies between zero (for $i = p$) to a small number $n_i \ll p$.

We choose a linear Gaussian model

$$p(h_i) = \mathcal{N}(h_i|\mathbf{l}_i^\top \widetilde{\mathbf{h}}_i, w_{hi}^{-1}), \tag{13}$$

where $\mathbf{l}_i$ is a vector of unknown correlations of length n_i and w_{hi} is the unknown precision (inverse variance). Model 13 corresponds to

$$h_{hi} = -\sum_{j=1}^{n_i} l_{h,j}\widetilde{h}_{hj} + w_{hi}^{-\frac{1}{2}}e_i, e_i \sim \mathcal{N}(0, 1) \tag{14}$$

In multivariate notation, it can be written as

$$\mathbf{h}_h = -\widetilde{\mathbf{L}}_h^\top \mathbf{h}_h + \mathbf{W}_h^{-\frac{1}{2}}\mathbf{e}, \tag{15}$$

$$(\mathbf{I}_p + \widetilde{\mathbf{L}}_h^\top)\mathbf{h}_h = \mathbf{W}_h^{-\frac{1}{2}}\mathbf{e}, \tag{16}$$

where $\widetilde{\mathbf{L}}_h$ is (generally sparse) lower triangular matrix where correlation coefficients $\mathbf{l}_{hi}$ are located in the $i$the column of $\widetilde{\mathbf{L}}_h$ at indexes given by $\mathscr{I}_i$, and $\mathbf{W}_h$ is a diagonal matrix such that

$$\mathbf{W}_h = \text{diag}(\mathbf{w}_h) = \begin{pmatrix} w_{h1} & & & \\ & w_{h2} & & \\ & & \ddots & \\ & & & w_{hp} \end{pmatrix} \tag{17}$$

Defining $\mathbf{L}_h = \widetilde{\mathbf{L}}_h + \mathbf{I}_p$ and using transformation of variables, 16 can be rewritten as zero mean Gaussian with covariance matrix $\Sigma_{h0}^{-1} = \mathbf{L}_h \mathbf{W}_h \mathbf{L}_h^T$. Combining this derivation with the assumption of bounded corrections 8, we obtain the final prior distribution in the form of the truncated

Gaussian distribution

$$p(\mathbf{h}_h|\Sigma_{h0}) = t\mathcal{N}(\mathbf{h}_h|\mathbf{0}, \Sigma_{h0}, [-\Delta s_h, \Delta s_h])$$

$$\propto \begin{cases} \exp\left(-\frac{1}{2}\mathbf{h}_h^T\Sigma_{h0}^{-1}\mathbf{h}_h\right), \text{if}\,\mathbf{h}_h \in [-\Delta s_h, \Delta s_h], \\ \\ 0 \qquad\qquad\qquad\qquad \text{otherwise.} \end{cases} \tag{18}$$

which is defined properly in Appendix A and where symbol $\propto$ denotes equality up to normalizing constant. While it may look as a common Gaussian prior, the trick is in the structure of the covariance matrix, which allows efficient estimation of its coefficients $\mathbf{L}_h$ and $\mathbf{W}_h$. It is a generalization of the sparsity and smoothness prior (Tichý et al., 2016).

The number of non-zero elements of matrix $\mathbf{L}_h$ depends on the choice of the neighborhood. Specifically, the jth measurement y_j belongs to $\mathscr{I}_i$ when the spatial distance between ith measurement and jth measurement locations is less than given distance and the time distance between ith measurement and jth measurement less than given period.

2.3.2. Prior model of elastic coefficients

The probabilistic model is completed by definition of the prior distribution of the unknown parameters $\mathbf{L}_h$ and $\mathbf{W}_h$ (and analogically of $\mathbf{L}_v$, $\mathbf{W}_v$, $\mathbf{L}_t$ and $\mathbf{W}_t$). The prior distribution for the vector $\mathbf{w}_h$ is Gamma distribution, similarly to previous noise model 10,

$$p(w_{hi}) = \mathcal{G}_{w_{hi}}\left(w_{hi}|\kappa_0^h, \nu_0^h\right), \quad \forall i, \tag{19}$$

where, again, κ_0^h and ν_0^h are prior constants selected as non-informative 10^{-10}. Since we prefer low number of corrections, the prior distribution for elastic coefficients vectors $\mathbf{l}_{hi}$ is selected to favor sparse solution, i.e. with diagonal precision matrix $\text{diag}(\varsigma_{hi})$ which is estimated together with the other variables as

$$p(\mathbf{l}_{hi}|\varsigma_{hi}) = \mathcal{N}\left(\mathbf{l}_{hi}|\mathbf{0}, \text{diag}(\varsigma_{hi})^{-1}\right), \quad \forall i, \tag{20}$$

$$p(\varsigma_{hi,j}) = \mathcal{G}\left(\varsigma_{hi,j}|\zeta_0, \eta_0\right), \quad \forall i, \forall j \in 1, \ldots, n_i, \tag{21}$$

where prior constants ζ_0 and η_0 are selected as 10^{-2} which allows parameter $\mathbf{l}_{hi}$ vary in the range approximately 0 ± 100 which is considered sufficient (Tichý et al., 2016).

The prior models for two other weighting vectors, $\mathbf{h}_v$ and $\mathbf{h}_t$, are identical as for the vector $\mathbf{h}_h$.

2.3.3. Prior model of the source term

We consider two potential prior models of the source term: (i) the LSAPC prior (Tichý et al., 2016), and (ii) the optimization-based approach of Eckhardt et al. (2008). LSAPC prior model for $p(\mathbf{x}|\mathbf{l}_x, \mathbf{w}_x, \varsigma_x)$ has hyper-parameters $\mathbf{l}_x, \mathbf{w}_x, \varsigma_x$ of the same distributions as 19–21. The tuning parameters of the optimization approach are selected by the designer and are thus not estimated.

2.4. Variational Bayes solution

The solution of the formulated prior model of the elastic bias field correction is based on the variational Bayes methodology (Smidl and Quinn, 2006) which seeks for approximation in the form of conditional independent posteriors. It is shown that the optimal solution minimize the Kullback-Leibler divergence (Kullback and Leibler, 1951) between the posterior and the hypothetical true parameters distribution. This results in the form of approximate posterior as

$$\widetilde{p}(\theta_i|\mathbf{y}) \propto \exp\left(\mathbb{E}_{\widetilde{p}(\theta_{/i}|\mathbf{y})}(\ln p(\theta, \mathbf{y}))\right), \quad \forall i, \tag{22}$$

where θ_i denotes ith variable from the set of all considered variables, $\theta_{/i}$ denotes complement of θ_i in θ, and $\mathbb{E}()$ denotes expected value of given argument. The Eq. 22 forms a set of implicit equations which need to be

solved iteratively. This set is formulated in Appendix A and together with standard moments of respected distributions can be solved using iterative evaluation of the equations.

The full model 9–21 contains variables $\mathbf{x}$, $\mathbf{h}_h$, $\mathbf{h}_v$, $\mathbf{h}_t$ with hyper-parameters for the elastic coefficients $\mathscr{L} = \{\mathbf{l}_{h,i}, \mathbf{l}_{v,i}, \mathbf{l}_{t,i}\}_{i=1}^p$, $\mathscr{W} = \{\mathbf{w}_{h,i}, \mathbf{w}_{v,i}, \mathbf{w}_{t,i}\}_{i=1}^p$ and $\mathscr{S} = \{\varsigma_{h,i}, \varsigma_{v,i}, \varsigma_{t,i}\}_{i=1}^p$. Due to model structure, the hyperparameters of elastic coefficients are conditionally independent and the variational methodology allows very efficient estimation.

The full Variational Bayes solution will be used for the LSAPC source term models, since it fully fits into the framework, using equations from (Tichý et al., 2016). The only exception is the matrix $\mathbf{M}$ which is replaced by its expected $\langle\widetilde{\mathbf{M}}\rangle$. We will use notation $\langle\theta\rangle = \int\theta_i\widetilde{p}(\theta_i|\mathbf{y})d\theta_i$ to denote expectation of its argument with respect to its posterior factor. Also, product M^TM is replaced by $\langle\widetilde{\mathbf{M}}^T\widetilde{\mathbf{M}}\rangle$. Solution of the model is based on iterative scheme that cyclically evaluates equations of the shaping parameters given in Appendix A.

2.5. Combination with arbitrary source term determination method

In this Section, we provide an algorithm for estimation of the bias correction for an arbitrary source term determination model. We assume that for a given bias corrected matrix $\widetilde{\mathbf{M}}$ the method can provide a distribution $p(\mathbf{x}|\widetilde{\mathbf{M}}, y)$. Note that it includes methods providing point estimates, since it can be interpreted as a Dirac distribution. Under this special choice, minimization of the KL divergence is equivalent to the expectation-maximization (EM) algorithm (Dempster et al., 1977), where the proposed bias correction estimate provides the E-step, while the source term determination method provides the M-step.

In practical terms, the resulting scheme is an algorithm iterating two blocks: (i) source term determination, and (ii) bias correction. The source term determination method provides the expected value of the source term $E(\mathbf{x}) \equiv \langle\mathbf{x}\rangle$. The input of the source term estimation is the corrected SRS matrix $\widetilde{\mathbf{M}}$ and measurement $\mathbf{y}$. The estimated $\langle\mathbf{x}\rangle$ is input to the bias correction block (Appendix A) that will yield the updated estimate of the corrected SRS matrix $\widetilde{\mathbf{M}}$. The whole approach is summarized in Fig. 4.

The use of this algorithm has been demonstrated on the *optimization method* of Eckhardt et al. (2008)) where cost function imposing combination of the Tikhonov regularization term and the smoothness of the source term $\mathbf{x}$ is used. Indeed, any other source term estimation method can be used within this scope.

Reference implementation of the elastic plume bias correction method, see Table 1, can be downloaded from: https://github.com/ond rej-tichy/BiasCorr/.

3. Results

We demonstrate the effects of the elastic plume bias correction methodology on two source term estimation methods from Section 2.5, the LSAPC and the optimization method, summarized in Table 1. We study two real world continental scale datasets. First, the European Tracer Experiment (ETEX) (Nodop et al., 1998) with known source term and fine resolution of measurements is used to validate the proposed bias correction and its interoperation with the source term determination methods. Second, the ^{106}Ru occurrence over Europe in 2017 (Masson et al., 2019) is used to demonstrate the effect of the bias correction to a much more demanding case without the known source term. Moreover, we tested the method for both, forward (the ETEX case) and backward (the ^{106}Ru case), runs of atmospheric transport model.

3.1. European Tracer Experiment (ETEX)

The ETEX is one of a few large scale controlled releases with all available measurements and source term of the release published
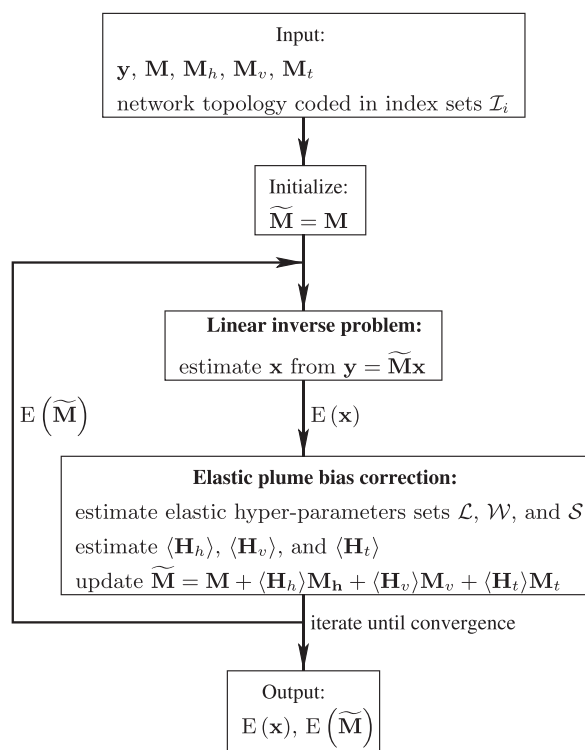

Fig. 4. The computational scheme of the elastic plume bias correction coupled with an arbitrary linear inverse algorithm. The hyper-parameters sets are defined as $\mathscr{L} = \{\mathbf{l}_{h,i}, \mathbf{l}_{v,i}, \mathbf{l}_{t,i}\}_{i=1}^p$, $\mathscr{W} = \{\mathbf{w}_{h,i}, \mathbf{w}_{v,i}, \mathbf{w}_{t,i}\}_{i=1}^p$, and $\mathscr{S} = \{\varsigma_{h,i}, \varsigma_{v,i}, \varsigma_{t,i}\}_{i=1}^p$. Each hyper-parameter has its posterior distribution expressed as a function of its shaping parameters, e.g. hyper-parameter $\mathbf{l}_{h,i}$ is defined by shaping parameters $\mu_{\mathbf{l}_{hi}}$ and $\Sigma_{\mathbf{l}_{hi}}$, which are given in Appendix A.

Table 1
Nomenclature of the tested methods.

Methodology for linear inversion	Linear inverse method	Bias correction with linear inversion
Tichý et al. (2016))	LSAPC	BiasCorr-LSAPC
Eckhardt et al. (2008))	Optimization	BiasCorr-Optim

(Nodop et al., 1998) and, therefore, is widely used for methodology validation. In this paper, we consider the first ETEX release where a total of 340 kg of nearly inert perfluoromethylcyclohexane (PMCH) was released during nearly 12 h at the constant rate at Monterfil in Brittany, France, on 23 October 1994. The atmospheric concentration measurements were collected from 168 measuring stations across the Europe with the sampling interval 3 h. In total, 3104 valid measurements were reported.

3.1.1. Atmospheric modeling and the bias correction algorithm settings

To obtain SRS fields for the ETEX release, we use the HYSPLIT atmospheric transport model (Stein et al., 2015; Draxler and Hess, 1997) in the forward mode driven by meteorological input data from the European Center for Medium-Range Weather Forecasts (ECMWF) ERA-Interim reanalysis (Dee et al., 2011) with spatial resolution 0.5 degree. The spatial domain is selected to cover all measuring stations as 40–65 degrees in latitude and − 5–30 degrees in longitude and with 1 h temporal resolution of the output grid. The SRS readings occur from 22 October to 27 October, i.e. 144 h are studied to properly surround the true release.

For the elastic bias corrections, we consider 0.5 degree spatial surroundings of each measurement station, i.e. the considered longitudinal and latitudinal shift, Δs_h and Δs_v. For time shift, Δt, we consider 1 h shift

forward and backward in time for each measurement. To deal with boundary conditions for time shifts, we shorten the assumed temporal interval by one step from each end to 142 h which still sufficiently cover the release. We end up with the nominal SRS matrix $\mathbf{M}$ of the size 3104×142 and gradient matrices $\mathbf{M}_h$, $\mathbf{M}_v$, and $\mathbf{M}_t$ of the same size representing local sensitivity for each measurement. For construction of index matrices $\mathscr{I}_i$ of sparse shapes of matrices $\mathbf{L}_h$, $\mathbf{L}_v$, and $\mathbf{L}_t$, we consider that two measurements neighboring if their spatial distance is less than 1.0 degree and temporal distance is less than 3 h. These are inputs for the elastic plume bias correction algorithm, Fig. 4.

3.1.2. Results and discussion

The key advantage of the ETEX experiment is that the true source term is known, see Fig. 6, top left panel where the true release is displayed using dashed red line. To test and validate the bias correction itself, we substitute the true source term in model 5 to obtain a linear model for the bias correction (Remark 1). The estimated bias correction for the true release at example time step $T + 17$ is given in Fig. 5, left column. Locations of all non-zero measurements are displayed using black dots and the release site is displayed using blue cross. The bias corrections are displayed using arrows for space coordinates of the bias and color for the time coordinate (blue arrows denote forward time shift and red denote backward time shift). In the top panels, the arrows are six-times enlarged for better visibility since the length of the correction is limited to 0.5 degree which is too small in this scale. The true scale of the estimated bias is used in the zoomed area in the bottom panels in Fig. 5. Agreement of the model with measurements is displayed in the top row of Fig. 6 using scatter plots of the model prediction against the measurements. The more closer to the axis of the first quadrant are the points on scatter plot, the better agreement between the model predictions and measurements is achieved. The improvement is indicated also using coefficient of determination, R^2, defined as

$$R^2 = 1 - \frac{\sum_i \left(y_i - (\mathbf{M}\langle\mathbf{x}\rangle)_i\right)^2}{\sum_i (y_i - \bar{y})^2}, \tag{23}$$

where $\bar{y}$ denotes mean of the measurements, with R^2 equal to 0 being nominal value and R^2 equal to 1 being the best fit. While for the nominal model, the agreement of the predictions using the true source term is poor ($R^2 = -1.6$), the agreement with the bias corrected predictions is much better with $R^2 = 0.65$. The estimated bias correction for the linear model with the true source term will be used in comparisons with the estimates of the bi-linear model.

Results of both algorithms for joint estimation of the bias correction

and the source term are displayed in Fig. 5 (bias correction) and Fig. 6 (source terms). Note that the bias correction fields for the BiasCorr-LSAPC (Fig. 5 middle) and the BiasCorr-Optim (Fig. 5 right) are very similar to those estimated using the true source term. For example, note the pattern in Hungary that systematically shifts the predicted plume to the north-west in the top panels. Moreover, Fig. 5 demonstrates the elasticity of the bias field correction where abrupt changes in the bias direction are less probable due to correlated directions in the neighborhood. In general, the proposed algorithm increases the correlation coefficients around the estimated shifts that are correlated, increasing pressure on the neighboring biases to align with them. In effect, the neighboring corrections are very often correlated forming clusters with corrections favoring one spatial direction and temporal shift direction.

The estimated field corrections have also positive impact on the estimated source terms. The true and the estimated source terms are given in Fig. 6 where the true release (best seen in the first row) is displayed by dashed red line and the estimated releases using the LSAPC (the second row) and the optimization (the third row) methods are displayed by blue lines. Each row in the plot displays results of estimation for the nominal model (left columns) and the joint estimation with the bias correction (right column). Similarly to improvement for the scatter plot of the linear model with true source term, the agreement of the model predictions with measurements of the bi-linear estimates has also improved. In fact, the bi-linear model estimates achieve higher R^2 than those with the known true release. Importantly, the shapes of scatter plots improved significantly, concentrating most of points around axis of the first quadrant. This is a consequence of higher number of parameters of the bi-linear model, indicating a minor over-fitting of the bi-linear models. This is not surprising due to poor conditioning of the inverse task. Note that all models achieved almost perfect agreement with the four highest measurements. The points where the agreement was not reached are also very similar in all methods. This may indicate that the true plume bias was higher than the limits imposed in the regularization. The estimated source terms for bi-linear models are also closer to the true release than those estimated using the nominal model.

Detailed comparison of measurements and reconstructions are displayed using mapping toolbox (Greene et al., 2019) in Fig. 7. The measurements are used as the reference with which we compare reconstructions for all six tested methods (including those using the true source term). The size of the circle is used to denote concentration value and the color is used to denote agreement with the measurement, see two legends in the bottom of Fig. 7. For better interpretation of the results, we also accompanied each map with the table of statistics of the number of reconstructions within factors 1.0–1.5, 1.5–2.0, 2.0–3.0, and
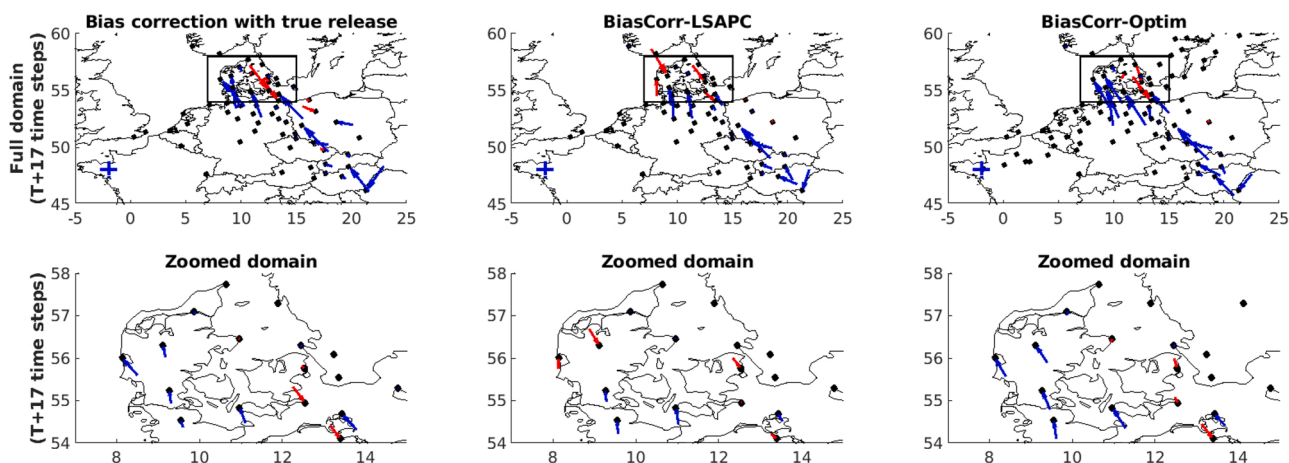

Fig. 5. The exact bias correction fields are demonstrated for tested methods for particular times step (T + 17) where stations with non-zero measurements are displayed using black dots and the release site using blue cross. The full spatial domain is given in the first row with enlarged arrows for better visibility, i.e. directions of bias corrections are given. The zoomed domain is given in the second row with true-scale arrows indicating bias correction using starts of each arrow. The coloring of arrows indicates the forward (blue) or backward (red) temporal shift of the SRS field.
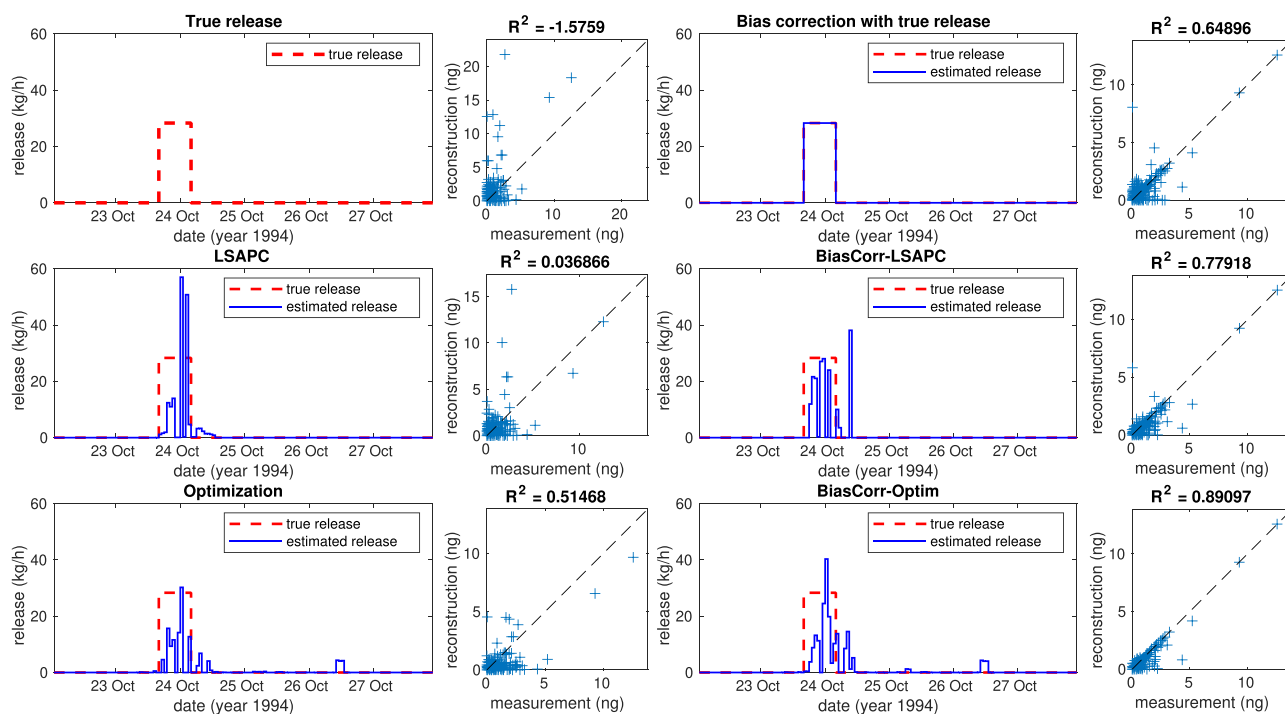
Fig. 6. The true (dashed red lines) and estimated (full blue lines) releases from the ETEX experiment using methods given in titles. Each plot is associated (on the left side) with the scatter plot between measurements and reconstruction with computed R^2 value.

higher than 3.0. In all cases, these tables demonstrate better agreement between measurements and results of bias corrected estimates than agreement between measurements and results using nominal model.

To conclude the results on the ETEX experiment, we have demonstrated that even small biases in the atmospheric transport model cause significant mismatch between measurements and model prediction. The proposed bias correction method can reduce this disproportion using information about gradients of concentration in the neighborhood of each measuring site. The proposed bias field correction is thus not based on ad hoc assumptions but reflects the numerical model and measurement network topology to provide elastic transformation of the concentrations.

3.2. Ruthenium-106 release in 2017

The occurrence of low concentrations of ^{106}Ru in Europe in September/October of 2017 is of particular interest in scientific community in recent years. Although the concentrations were low and pose no radiological risk, the origin of ^{106}Ru is questioned. There were several hypotheses: a nuclear reactor accident was rejected because other radionuclides were not detected so as release from medical applications since it does not explain such a large source of ^{106}Ru. Therefore, fresh nuclear fuel was considered as the most probable source due to the observation of ratio between ^{106}Ru and ^{103}Ru (Masson et al., 2019), probably from a fuel reprocessing plant. Multiple investigations have been performed and the Mayak plant (South Ural, Russian Federation) have been selected as the most probable source (Masson et al., 2019; Saunier et al., 2019; De Meutter et al., 2021; Dumont Le Brazidec et al., 2020; Tichý et al., 2021), although Russian authorities did not confirm this findings. In this study, we assume that the location of the ^{106}Ru release is the Mayak reprocessing plant. We use the largest dataset on this release from Masson et al. (2019)) and perform bias correction coupled with source term estimation methods similar to the previous case of ETEX release. Although the source term is not known, we compare our results with already published findings.

3.2.1. Atmospheric modeling and bias correction algorithm settings

FLEXPART version 10.4 (Pisso et al., 2019) was used in backward mode to calculate the SRS matrices needed for the bilinear model. FLEXPART releases computational particles that are tracked in time following 3-hourly operational meteorological analyses from the European Center for Medium-Range Weather Forecasts (ECMWF) with 137 vertical layers and a spatial resolution of 1×1 degree. The model accounts for dry and wet deposition (Grythe et al., 2017), turbulence (Cassiani et al., 2015), unresolved mezoscale motions (Stohl et al., 2005), and convection (Forster et al., 2007). The spatial domain was selected as 30–75 degree in latitude and as -10–100 in longitude to cover all measuring stations. The temporal domain is selected from 2 August to 10 October 2017 (due to few long measurements times) with 3 h temporal resolution of the output grid yielding 557 temporal elements. The SRS matrices $\mathbf{M}$, $\mathbf{M}_h$, $\mathbf{M}_v$, and $\mathbf{M}_t$ were calculated for the Mayak location backward in time, at temporal intervals that matched measurements at each receptor site. ^{106}Ru is tracked assuming gravitational settling for spherical particles with an aerosol mean diameter of 0.6 μm and a normalized standard deviation of 3.3 and a particle density of 2500 kg m^{-3} (Masson et al., 2019).

For bias field corrections, we assume 1.0 degree spatial surroundings for each measuring station and 3 h temporal surroundings for each measurement. For construction of sparse shapes of matrices $\mathbf{L}_h$, $\mathbf{L}_v$, and $\mathbf{L}_t$, we consider that two measurements neighboring if they spatial distance is less than 2.0 degrees and temporal distance is less than 3 h.

3.2.2. Results and discussion

Since we can not compare the results with the ground truth, we show only impact of the bias correction of the estimates of the source term in Fig. 8. Here, the first two columns display results from the linear LSAPC and optimization methods and the next two columns display results for bi-linear model with the bias correction. In all cases, we display the estimated source term with 3 h discretization together with the associated scatter plot between measurements and reconstructions and with computed R^2 values. Note that the temporal interval of the displayed source term is cropped to focus on non-zeros estimated activity while in
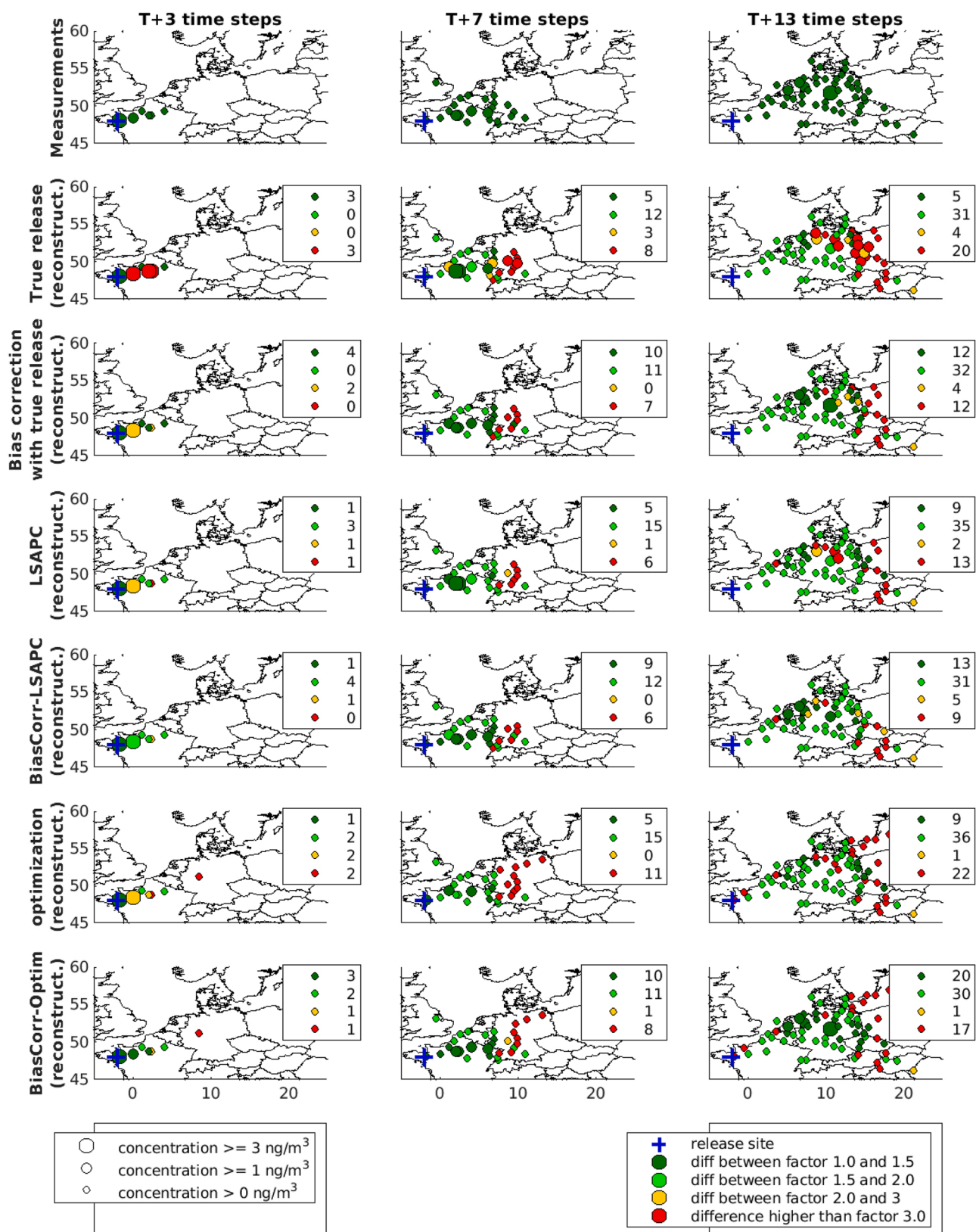
Fig. 7. Measurements are shown in the first row. Other rows show a comparison between measurements and reconstructions using specified methods for three selected time steps (in columns). The size of each bullet indicates the measured/reconstructed value while the color of each bullet indicates the agreement between the measurement and the reconstructed value, see legends for details. Each map contains legend with the sum of bullets with given type of coloring for easier comparison.
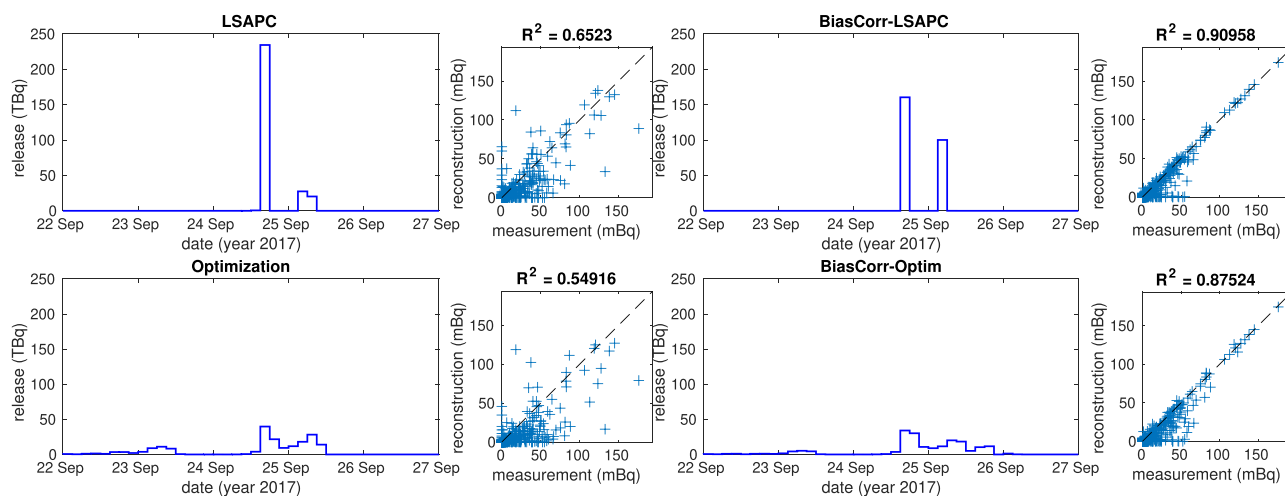
Fig. 8. The estimated releases of ^{106}Ru using methods given in titles are given using full blue lines. Each plot is associated (on the left side) with the scatter plot between measurements and reconstruction with computed R^2 value.

the rest of the time domain, the releases are estimated as zeros. In all cases, we estimated the majority of the release between 24 September and 25 September while the total estimated release is 283 TBq for the LSAPC method, 261 TBq for the BiasCorr-LSAPC method, 200 TBq for the optimization method, and 195 TBq for the BiasCorr-Optim method. The main difference between the results with and without bias correction is in mass distribution of the release. Higher releases were observed on 25 September for the bias correction method than without bias correction. Although the LSAPC method provides sparser estimates than the optimization method, we observe clearly two main peaks of release in all cases, supporting the hypothesis that the release was not unimodal but had two or three peaks (see also small activity in 23 September in the case of optimization method). This supports the findings of Saunier et al. (2019)) where release of the magnitude less than 2 TBq in 23 September and even small one in 24 September was reported. Although we have no true source term, we can compare our findings with other published results. The main release was estimated by Western et al. (2020)) to 24 September as 441 TBq and by Dumont Le Brazidec et al. (2021)) mainly to 25 September with release between 200 and 450 TBq, while other methods mostly estimated 25 and 26 September with activity 250 TBq (Saunier et al., 2019), 500 TBq (Shershakov et al., 2019), 237 TBq (Tichý et al., 2021), and between 100 and 200 TBq (Dumont Le Brazidec et al., 2020), based on the used prior model. Our findings are in agreement in terms of the temporal resolution of the releases as our releases were estimated between 24 and 25 September. This also agrees regarding total released activity that results in the best R^2 value for modelled and measured concentrations obtained using the BiasCorr-LSAPC method (total release activity of 261 TBq).

The examples of detailed measurements reconstructions are given in Fig. 9 for given times specified in titles. The size of each bullet indicates the value of measurement (top row) or reconstruction (second to fifth rows) and the coloring indicates the difference of the reconstruction from the measurement, see legends bellow. As in the case of ETEX, we also computed the number of reconstructions differing from measurements by factor 1.5, 2, 3, and more than 3, see legend given for each panel. Here, the improvement of reconstruction with the use of the bias correction is demonstrated in all cases. Also, Fig. 9 demonstrates slightly better reconstruction using the BiasCorr-LSAPC method than using the BiasCorr-Optim method, the third and the fifth rows. In the latter case, there are significantly miss-reconstructed values in the northern Germany and the southern Norway which is not the case of the former case. This results in slightly higher R^2 value in the former case. This is probably caused by the more smooth estimates using optimization leaving the residual activity in subsequent reconstruction which is not the case

for the LSACP method where we observe two separated releases. This supports the hypothesis that there were two releases of ^{106}Ru with similar strength approximately 9 h in a row. Notably, the bias correction algorithm was able to reduce the disproportion between measurements and reconstructions significantly in both cases.

4. Conclusions

We propose a method for improved estimation of the source term via better estimation of the plume bias. Our bias correction method uses not only concentrations modeled at measuring stations but also the information from the neighborhood of each measuring station in the form of SRS coefficients. This provide quantitatively better information than other previous approaches which use the modeled point concentrations only. The proposed bias correction method is based on elastic transformation of the SRS fields while the regularization of the correction is based on knowledge on the topology of the measuring network. Since all information necessary for the proposed bias correction is already available from the atmospheric transport model and the method can be combined with an arbitrary linear inverse method that uses the SRS matrix, the bias correction is widely applicable for improvement of estimation of the source term of atmospheric releases.

The performance of the proposed method was studied in two real cases. First, we use data from the European Tracer Experiment (ETEX) where the true source term is known. We demonstrate that bias corrections estimated without the knowledge of the true source term are very similar to those bias corrections estimated with the use of the true source term. Second, we study the case of occurrence of ^{106}Ru over Europe in the fall of 2017. In this demanding case, we demonstrate that the method can correct atmospheric transport model biases and can significantly better explain the concentration measurements than linear inverse methods alone.

We conclude that the proposed bias correction method provides general, effective, and flexible framework which can, coupled with a selected linear inverse method, reduce the model bias and provide more accurate estimate of the source term of an atmospheric release.

CRediT authorship contribution statement

Ondřej Tichý: Methodology, Lagrangian modelling, Inverse modelling algorithm development, Investigation, Writing – review and editing. **Václav Šmídl:** Methodology, Inverse modelling algorithm development, Writing – review & editing. **Nikolaos Evangeliou:** Lagrangian modelling, Writing – review & editing.
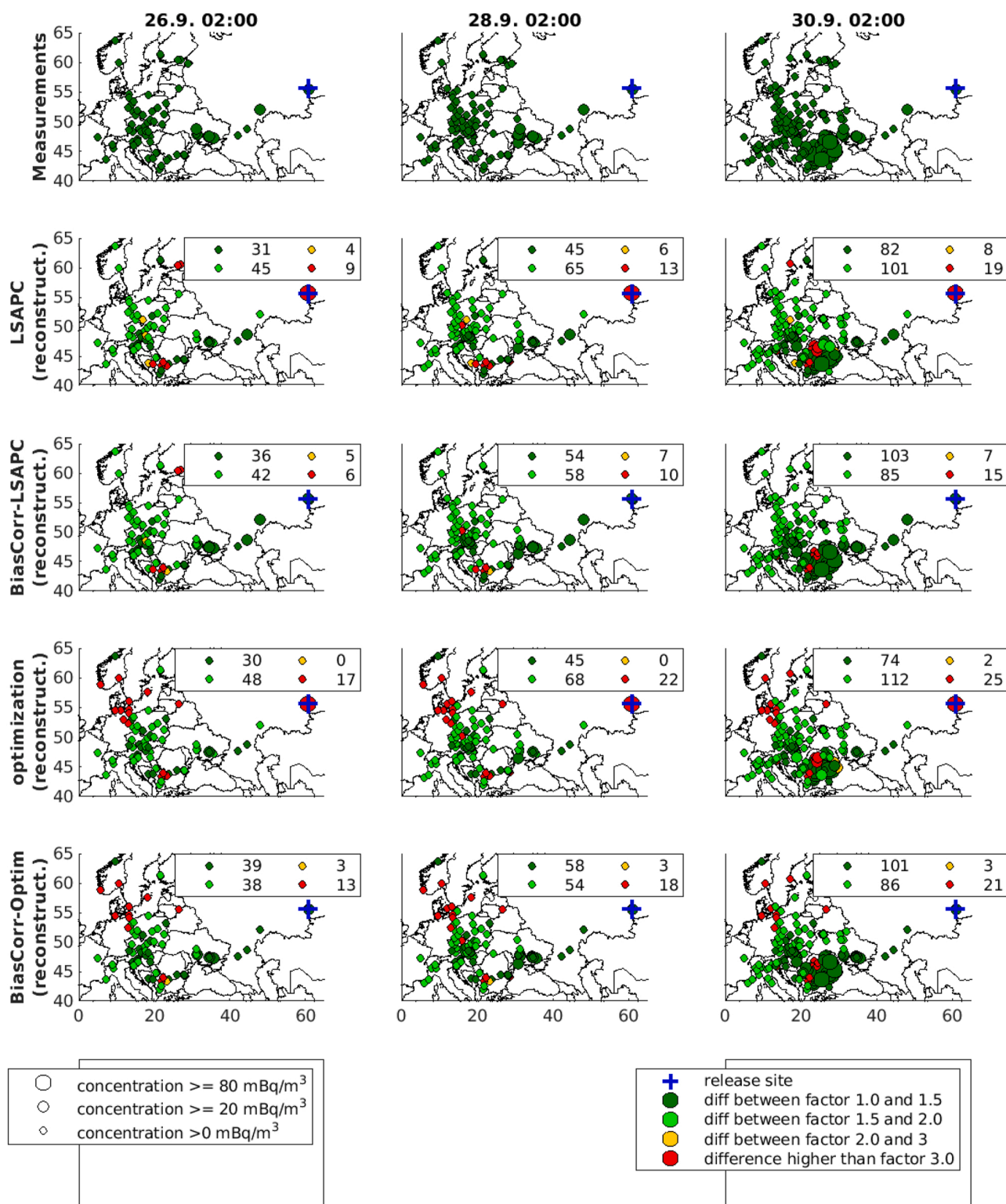
Fig. 9. The comparison between measurements (first row) and reconstructions using specified methods for three selected time steps (in columns). The size of each bullet indicates the measured/reconstructed value while the color of each bullet indicates the agreement between the measurement and the reconstructed value, see legends for details. Each map contains legend with the sum of bullets with given type of coloring for easier comparison.

Declaration of Competing Interest

The authors declare that they have no known competing financial interests or personal relationships that could have appeared to influence the work reported in this paper.

Appendix A. Truncated Gaussian distribution

Truncated Gaussian distribution, denoted as $t\mathcal{N}$, of a scalar variable x on interval $[a;b]$ is defined as

$$t\mathcal{N}_x(\mu, \sigma, [a,b]) = \frac{\sqrt{2}\exp((x-\mu)^2)}{\sqrt{\pi}\sigma(\mathrm{erf}(\beta) - \mathrm{erf}(\alpha))}\chi_{[a,b]}(x), \tag{24}$$

where $\alpha = \frac{a-\mu}{\sqrt{2}\sigma}$, $\beta = \frac{b-\mu}{\sqrt{2}\sigma}$, function $\chi_{[a,b]}(x)$ is a characteristic function of interval $[a,b]$ defined as $\chi_{[a,b]}(x) = 1$ if $x \in [a,b]$ and $\chi_{[a,b]}(x) = 0$ otherwise. $\mathrm{erf}()$ is the error function defined as $\mathrm{erf}(t) = \frac{2}{\sqrt{\pi}}\int_0^t e^{-u^2}\,\mathrm{d}u$.

The moments of truncated normal distribution are

$$\langle x \rangle = \mu - \sqrt{\sigma}\,\frac{\sqrt{2}[\exp(-\beta^2) - \exp(-\alpha^2)]}{\sqrt{\pi}(\mathrm{erf}(\beta) - \mathrm{erf}(\alpha))}, \tag{25}$$

$$\langle x^2 \rangle = \sigma + \mu\widehat{x} - \sqrt{\sigma}\,\frac{\sqrt{2}[b\exp(-\beta^2) - a\exp(-\alpha^2)]}{\sqrt{\pi}(\mathrm{erf}(\beta) - \mathrm{erf}(\alpha))}. \tag{26}$$

Appendix B. Shaping parameters of posterior distributions of bias correction

Here, we provide posterior distributions and associated shaping parameters for the longitudinal bias correction, with subscript h. The posterior distribution and shaping parameters for the latitudinal and temporal bias correction are analogical while the full bias correction method is available online.

The posterior distributions for longitudinal bias correction are identified as

$$\widetilde{p}(\mathbf{h}_h|\mathbf{y}) = t\mathcal{N}\left(\mathbf{h}_h\big|\mu_{\mathbf{h}_h}, \Sigma_{\mathbf{h}_h}, [-\Delta s_h, \Delta s_h]\right), \tag{27}$$

$$\widetilde{p}(\mathbf{w}_h|\mathbf{y}) = \mathcal{G}\left(\mathbf{w}_h\big|\kappa^h, \nu^h\right), \tag{28}$$

$$\widetilde{p}(\mathbf{l}_{hi}|\mathbf{y}) = \mathcal{N}\left(\mathbf{l}_{hi}\big|\mu_{\mathbf{l}_{hi}}, \Sigma_{\mathbf{l}_{hi}}\right), \quad \forall i, \tag{29}$$

$$\widetilde{p}(\varsigma_{hi}|\mathbf{y}) = \mathcal{G}\left(\varsigma_{hi}\big|\xi_i^h, \eta_i^h\right), \quad \forall i, \tag{30}$$

$$\widetilde{p}(\omega|\mathbf{y}) = \mathcal{G}(\omega|\vartheta, \rho) \tag{31}$$

The posterior distributions are functions of their shaping parameters, $\mu_{\mathbf{h}_h}, \Sigma_{\mathbf{h}_h}, \kappa^h, \nu^h, \mu_{\mathbf{l}_{hi}}, \Sigma_{\mathbf{l}_{hi}}, \xi_i^h, \eta_i^h, \vartheta, \rho$, which follows:

$$\Sigma_{\mathbf{h}_h} = (\,)\langle\omega\rangle\mathrm{diag}\,\mathrm{diag}\left(\mathbf{M}_h\langle\mathbf{xx}^T\rangle\mathbf{M}_h^T\right) + \\ + \langle\mathbf{L}_h\mathrm{diag}\left(\mathbf{w}^h\right)\mathbf{L}_h^T\rangle)^{-1}, \tag{32}$$

$$\mu_{\mathbf{h}_h} = \Sigma_{\mathbf{h}_h}\langle\omega\rangle(\,)\mathrm{diag}\left(\mathbf{M}_h\langle\mathbf{x}\rangle\mathbf{y}^T\right) + \\ -\mathrm{diag}\left(\mathbf{M}_h\langle\mathbf{xx}^T\rangle\mathbf{M}^T\right) + \\ -\mathrm{diag}\left(\langle\mathbf{H}_\nu\rangle\mathbf{M}_\nu\langle\mathbf{xx}^T\rangle\mathbf{M}_h^T\right) + \\ -\mathrm{diag}\left(\langle\mathbf{H}_t\rangle\mathbf{M}_t\langle\mathbf{xx}^T\rangle\mathbf{M}_h^T\right)), \tag{33}$$

$$\kappa^h = \kappa_0^h + \frac{1}{2}\mathbf{1}_{p,1}, \tag{34}$$

$$\nu^h = \nu_0^h + \frac{1}{2}\mathrm{diag}\left(\langle\mathbf{L}_h^T\mathbf{h}_h\mathbf{h}_h^T\mathbf{L}_h\rangle\right), \tag{35}$$

$$\Sigma_{\mathbf{l}_{hi}} = \left(\langle w_i^h\rangle\langle\mathbf{h}_{h,\mathscr{I}_i}\mathbf{h}_{h,\mathscr{I}_i}^T\rangle + \mathrm{diag}(\langle\varsigma_{hi}\rangle)\right)^{-1}, \tag{36}$$

$$\mu_{\mathbf{l}_{hi}} = \Sigma_{\mathbf{l}_{hi}}\left(-\langle w_i^h\rangle\langle h_{h,i}\mathbf{h}_{h,\mathscr{I}_i}^T\rangle\right), \tag{37}$$

$$\xi_i^h = \xi_0^h + \frac{1}{2}\mathbf{1}_{n_i}, \tag{38}$$

$$\eta_i^h = \eta_0^h + \frac{1}{2}\mathrm{diag}\left(\langle\mathbf{l}_{hi}\mathbf{l}_{hi}^T\rangle\right), \tag{39}$$

$$\vartheta = \vartheta_0 + \frac{p}{2}, \tag{40}$$

$$\rho = \rho_0 + \frac{1}{2}\mathrm{trace}\left(\langle\mathbf{xx}^T\rangle\langle\widetilde{\mathbf{M}}^T\widetilde{\mathbf{M}}\rangle\right) + \tag{41}$$

$$- \mathbf{y}^T \langle \widetilde{\mathbf{M}} \rangle \langle \mathbf{x} \rangle + \frac{1}{2} \mathbf{y}^T \mathbf{y}. \tag{42}$$

Here, the matrix $\widetilde{\mathbf{M}}$ is the corrected SRS matrix $\widetilde{\mathbf{M}} = \mathbf{M} + \langle \mathbf{H}_h \rangle \mathbf{M}_h + \langle \mathbf{H}_v \rangle \mathbf{M}_v + \langle \mathbf{H}_t \rangle \mathbf{M}_t$. The moments, denoted as $\langle \theta \rangle$, can be computed using standard equations for respected distributions, i.e. Gaussian, truncated Gaussian, and Gamma distributions.

References

Bocquet, M., 2012. Parameter-field estimation for atmospheric dispersion: application to the Chernobyl accident using 4D-Var. Q. J. R. Meteorol. Soc. 138, 664–681.

Cassiani, M., Stohl, A., Brioude, J., 2015. Lagrangian stochastic modelling of dispersion in the convective boundary layer with skewed turbulence conditions and a vertical density gradient: Formulation and implementation in the FLEXPART model. Bound. -Layer. Meteorol. 154, 367–390.

De Meutter, P., Hoffman, I., 2020. Bayesian source reconstruction of an anomalous Selenium-75 release at a nuclear research institute. J. Environ. Radioact. 218, 106225.

De Meutter, P., Hoffman, I., Ungar, K., 2021. On the model uncertainties in Bayesian source reconstruction using an ensemble of weather predictions, the emission inverse modelling system FREAR v1.0, and the Lagrangian transport and dispersion model Flexpart v9.0.2. Geosci. Model Dev. 14, 1237–1252. https://doi.org/10.5194/gmd-14-1237-2021.

Dee, D., Uppala, S., Simmons, A., Berrisford, P., Poli, P., Kobayashi, S., Andrae, U., Balmaseda, M., Balsamo, G., Bauer, P., Bechtold, P., Beljaars, A., van de Berg, L., Bidlot, J., Bormann, N., Delsol, C., Dragani, R., Fuentes, M., Geer, A., Haimberger, L., Healy, S., Hersbach, H., Hólm, E., Isaksen, L., Kallberg, P., Kohler, M., Matricardi, M., Mcnally, A., Monge-Sanz, B., Morcrette, J., Park, B., Peubey, C., de Rosnay, P., Tavolato, C., Thepaut, J., Vitart, F., 2011. The ERA-Interim reanalysis: Configuration and performance of the data assimilation system. Q. J. R. Meteorol. Soc. 137, 553–597.

Dempster, A., Laird, N., Rubin, D., et al., 1977. Maximum likelihood from incomplete data via the EM algorithm. J. R. Stat. Soc. 39, 1–38.

Draxler, R., Hess, G., 1997. Descr. HYSPLIT_4 Model. Syst.

Dumont Le Brazidec, J., Bocquet, M., Saunier, O., Roustan, Y., 2020. MCMC methods applied to the reconstruction of the autumn 2017 Ruthenium 106 atmospheric contamination source. Atmos. Environ.: X 6, 100071. https://doi.org/10.1016/j.aeaoa.2020.100071.

Dumont Le Brazidec, J., Bocquet, M., Saunier, O., Roustan, Y., 2021. Quantification of uncertainties in the assessment of an atmospheric release source applied to the autumn 2017 106Ru event. Atmos. Chem. Phys. 21, 13247–13267. https://doi.org/10.5194/acp-21-13247-2021.

Eckhardt, S., Prata, A., Seibert, P., Stebel, K., Stohl, A., 2008. Estimation of the vertical profile of sulfur dioxide injection into the atmosphere by a volcanic eruption using satellite column measurements and inverse transport modeling. Atmos. Chem. Phys. 8, 3881–3897.

Evangeliou, N., Hamburger, T., Cozic, A., Balkanski, Y., Stohl, A., 2017. Inverse modeling of the Chernobyl source term using atmospheric concentration and deposition measurements. Atmos. Chem. Phys. 17, 8805–8824.

Fang, S., Zhuang, S., Li, X., Li, H., 2021. Automated release rate inversion and plume bias correction for atmospheric radionuclide leaks: A robust and general remediation to imperfect radionuclide transport modeling. Sci. Total Environ. 754, 142140 https://doi.org/10.1016/j.scitotenv.2020.142140.

Forster, C., Stohl, A., Seibert, P., 2007. Parameterization of convective transport in a Lagrangian particle dispersion model and its evaluation. J. Appl. Meteorol. Climatol. 46, 403–422.

Ganesan, A.L., Rigby, M., Zammit-Mangion, A., Manning, A.J., Prinn, R.G., Fraser, P.J., Harth, C.M., Kim, K.R., Krummel, P.B., Li, S., Mühle, J., O'Doherty, S.J., Park, S., Salameh, P.K., Steele, L.P., Weiss, R.F., 2014. Characterization of uncertainties in atmospheric trace gas inversions using hierarchical Bayesian methods. Atmos. Chem. Phys. 14, 3855–3864.

Greene, C.A., Thirumalai, K., Kearney, K., Delgado, J., Schwanghart, W., Wolfenbarger, N., Thyng, K., Gwyther, D., Gardner, A., Blankenship, D., 2019. The climate data toolbox for matlab. Geochem., Geophys., Geosystems 20, 3774–3781.

Grythe, H., Kristiansen, N., Zwaaftink, C., Eckhardt, S., Ström, J., Tunved, P., Krejci, R., Stohl, A., 2017. A new aerosol wet removal scheme for the lagrangian particle model flexpart. Geosci. Model Dev. 10, 1447–1466.

Hutchinson, M., Oh, H., Chen, W.H., 2017. A review of source term estimation methods for atmospheric dispersion events using static or mobile sensors. Inf. Fusion 36, 130–148.

Katata, G., Ota, M., Terada, H., Chino, M., Nagai, H., 2012. Atmospheric discharge and dispersion of radionuclides during the Fukushima Dai-ichi nuclear power plant accident. Part I: Source term estimation and local-scale atmospheric dispersion in early phase of the accident. J. Environ. Radioact. 109, 103–113.

Kovalets, I., Tsiouri, V., Andronopoulos, S., Bartzis, J., 2009. Improvement of source and wind field input of atmospheric dispersion model by assimilation of concentration measurements: Method and applications in idealized settings. Appl. Math. Model. 33, 3511–3521.

Krysta, M., Bocquet, M., Sportisse, B., Isnard, O., 2006. Data assimilation for short-range dispersion of radionuclides: An application to wind tunnel data. Atmos. Environ. 40, 7267–7279.

Kullback, S., Leibler, R., 1951. On information and sufficiency. Ann. Math. Stat. 22, 79–86.

Kumar, K.P., Sundaram, G.S., Thiruvengadathan, R., 2020. Advances in detection algorithms for radiation monitoring. J. Environ. Radioact. 217, 106216.

Leelőssy, Á., Lagzi, I., Kovács, A., Mészáros, R., 2018. A review of numerical models to predict the atmospheric dispersion of radionuclides. J. Environ. Radioact. 182, 20–33.

Leelőssy, Á., Mészáros, R., Kovács, A., Lagzi, I., Kovács, T., 2017. Numerical simulations of atmospheric dispersion of iodine-131 by different models. PloS One 12, e0172312.

Li, X., Li, H., Liu, Y., Xiong, W., Fang, S., 2018. Joint release rate estimation and measurement-by-measurement model correction for atmospheric radionuclide emission in nuclear accidents: An application to wind tunnel experiments. J. Hazard. Mater. 345, 48–62.

Li, X., Sun, S., Hu, X., Huang, H., Li, H., Morino, Y., Wang, S., Yang, X., Shi, J., Fang, S., 2019. Source inversion of both long-and short-lived radionuclide releases from the Fukushima Daiichi nuclear accident using on-site gamma dose rates. J. Hazard. Mater. 379, 120770.

Ling, Y., Yue, Q., Huang, T., Shan, Q., Hei, D., Zhang, X., Jia, W., 2021. Multi-nuclide source term estimation method for severe nuclear accidents from sequential gamma dose rate based on a recurrent neural network. J. Hazard. Mater. 414, 125546 https://doi.org/10.1016/j.jhazmat.2021.125546.

Liu, Y., Haussaire, J.M., Bocquet, M., Roustan, Y., Saunier, O., Mathieu, A., 2017. Uncertainty quantification of pollutant source retrieval: comparison of Bayesian methods with application to the Chernobyl and Fukushima Daiichi accidental releases of radionuclides. Q. J. R. Meteorol. Soc. 143, 2886–2901.

Mao, S., Lang, J., Chen, T., Cheng, S., 2021. Improving source inversion performance of airborne pollutant emissions by modifying atmospheric dispersion scheme through sensitivity analysis combined with optimization model. Environ. Pollut. 284, 117186.

Mao, S., Lang, J., Chen, T., Cheng, S., Wang, C., Zhang, J., Hu, F., 2020. Impacts of typical atmospheric dispersion schemes on source inversion. Atmos. Environ. 232, 117572.

Martinez-Camara, M., BéjarHaro, B., Stohl, A., Vetterli, M., 2014. A robust method for inverse transport modeling of atmospheric emissions using blind outlier detection. Geosci. Model Dev. 7, 2303–2311.

Masson, O., Steinhauser, G., Wershofen, H., Mietelski, J.W., Fischer, H.W., Pourcelot, L., Saunier, O., Bieringer, J., Steinkopff, T., Hýža, M., Moller, B., Bowyer, T.W., Dalaka, E., Dalheimer, A., de Vismes-Ott, A., Eleftheriadis, K., Forte, M., GascoLeonarte, C., Gorzkiewicz, K., Homoki, Z., Isajenko, K., Karhunen, T., Katzlberger, C., Kierepko, R., Kovendiné Kónyi, J., Malá, H., Nikolic, J., Povinec, P. P., Rajacic, M., Ringer, W., Rulík, P., Rusconi, R., Sáfrány, G., Sykora, I., Todorovic, D., Tschiersch, J., Ungar, K., Zorko, B., 2018. Potential source apportionment and meteorological conditions involved in airborne 131I detections in January/February 2017 in Europe. Environ. Sci. Technol. 52, 8488–8500.

Masson, O., Steinhauser, G., Zok, D., Saunier, O., Angelov, H., Babić, D., Bečková, V., Bieringer, J., Bruggeman, M., Burbidge, C.I., Conil, S., Dalheimer, A., De Geer, L.E., de Vismes Ott, A., Eleftheriadis, K., Estier, S., Fischer, H., Garavaglia, M.G., GascoLeonarte, C., Gorzkiewicz, K., Hainz, D., Hoffman, I., Hýža, M., Isajenko, K., Karhunen, T., Kastlander, J., Katzlberger, C., Kierepko, R., Knetsch, G.J., KövendinéKónyi, J., Lecomte, M., Mietelski, J.W., Min, P., Møller, B., Nielsen, S.P., Nikolic, J., Nikolovska, L., Penev, I., Petrinec, B., Povinec, P.P., Querfeld, R., Raimondi, O., Ransby, D., Ringer, W., Romanenko, O., Rusconi, R., Saey, P.R.J., Samsonov, V., Šilobritiene, B., Simion, E., Söderström, C., Šoštarić, M., Steinkopff, T., Steinmann, P., Sýkora, I., Tabachnyi, L., Todorovic, D., Tomankiewicz, E., Tschiersch, J., Tsibranski, R., Tzortzis, M., Ungar, K., Vidic, A., Weller, A., Wershofen, H., Zagyvai, P., Zalewska, T., Zapata García, D., Zorko, B., 2019. Airborne concentrations and chemical considerations of radioactive ruthenium from an undeclared major nuclear release in 2017. Proc. Natl. Acad. Sci. 116, 16750–16759.

Nodop, K., Connolly, R., Girardi, F., 1998. The field campaigns of the European Tracer Experiment (ETEX): Overview and results. Atmos. Environ. 32, 4095–4108.

Pisso, I., Sollum, E., Grythe, H., Kristiansen, N.I., Cassiani, M., Eckhardt, S., Arnold, D., Morton, D., Thompson, R.L., GrootZwaaftink, C.D., Evangeliou, N., Sodemann, H., Haimberger, L., Henne, S., Brunner, D., Burkhart, J.F., Fouilloux, A., Brioude, J., Philipp, A., Seibert, P., Stohl, A., 2019. The Lagrangian particle dispersion model FLEXPART version 10.4. Geosci. Model Dev. 12, 4955–4997. https://doi.org/10.5194/gmd-12-4955-2019. ⟨https://gmd.copernicus.org/articles/12/4955/2019/⟩.

Saunier, O., Didier, D., Mathieu, A., Masson, O., Dumont Le Brazidec, J., 2019. Atmospheric modeling and source reconstruction of radioactive ruthenium from an undeclared major release in 2017. Proc. Natl. Acad. Sci. 116, 24991–25000.

Saunier, O., Mathieu, A., Didier, D., Tombette, M., Quélo, D., Winiarek, V., Bocquet, M., 2013. An inverse modeling method to assess the source term of the Fukushima nuclear power plant accident using gamma dose rate observations. Atmos. Chem. Phys. 13, 11403–11421.

Seibert, P., 2001. Iverse modelling with a lagrangian particle disperion model: application to point releases over limited time intervals. In: Air Pollution Modeling and its Application XIV. Springer, pp. 381–389.

Seibert, P., Frank, A., 2004. Source-receptor matrix calculation with a Lagrangian particle dispersion model in backward mode. Atmos. Chem. Phys. 4, 51–63.

Shershakov, V., Borodin, R., Tsaturov, Y., 2019. Assessment of possible location Ru-106 source in Russia in September-October 2017. Russ. Meteorol. Hydrol. 44, 196–202.

Šmídl, V., Quinn, A., 2006. The Variational Bayes Method in Signal Processing. Springer,.

Sørensen, J., Bartnicki, J., Buhr, A., Feddersen, H., Hoe, S., Israelson, C., Klein, H., Lauritzen, B., Lindgren, J., Schönfeldt, F., Sigg, R., 2020. Uncertainties in atmospheric dispersion modelling during nuclear accidents. J. Environ. Radioact. 222, 106356.

Stein, A., Draxler, R., Rolph, G., Stunder, B., Cohen, M., Ngan, F., 2015. NOAA's HYSPLIT atmospheric transport and dispersion modeling system. Bull. Am. Meteorol. Soc. 96, 2059–2077.

Stohl, A., Forster, C., Frank, A., Seibert, P., Wotawa, G., 2005. Technical note: The Lagrangian particle dispersion model FLEXPART version 6.2. Atmos. Chem. Phys. 5, 2461–2474.

Tichý, O., Hýža, M., Evangeliou, N., Šmídl, V., 2021. Real-time measurement of radionuclide concentrations and its impact on inverse modeling of ^{106}Ru release in the fall of 2017. Atmos. Meas. Tech. 14, 803–818. https://doi.org/10.5194/amt-2020-205.

Tichý, O., Šmídl, V., Hofman, R., Stohl, A., 2016. LS-APC v1.0: a tuning-free method for the linear inverse problem and its application to source-term determination. Geosci. Model Dev. 9, 4297–4311.

Tichý, O., Šmídl, V., Hofman, R., Šindelářová, K., Hýža, M., Stohl, A., 2017. Bayesian inverse modeling and source location of an unintended ^{131}I release in Europe in the fall of 2011. Atmos. Chem. Phys. 17, 12677–12696.

Tichý, O., Ulrych, L., Šmídl, V., Evangeliou, N., Stohl, A., 2020. On the tuning of atmospheric inverse methods: comparisons with the European Tracer Experiment (ETEX) and Chernobyl datasets using the atmospheric transport model FLEXPART. Geosci. Model Dev. 13, 5917–5934. https://doi.org/10.5194/gmd-13-5917-2020.

Western, L., Millington, S., Benfield-Dexter, A., Witham, C., 2020. Source estimation of an unexpected release of Ruthenium-106 in 2017 using an inverse modelling approach. J. Environ. Radioact. 220, 106304.

Zhang, X., Huang, M., 2017. Ensemble-based release estimation for accidental river pollution with known source position. J. Hazard. Mater. 333, 99–108.

Zhang, X., Li, Q., Su, G., Yuan, M., 2015. Ensemble-based simultaneous emission estimates and improved forecast of radioactive pollution from nuclear power plant accidents: application to ETEX tracer experiment. J. Environ. Radioact. 142, 78–86.

Zhang, X., Raskob, W., Landman, C., Trybushnyi, D., Li, Y., 2017. Sequential multi-nuclide emission rate estimation method based on gamma dose rate measurement for nuclear emergency management. J. Hazard. Mater. 325, 288–300.